Chapter 9

Phase Referencing

Andreas Quirrenbach

University of California, San Diego
La Jolla, California

9.1 Introduction

The use of phases in ground-based astronomical interferometry is severely limited by the pathlength fluctuations of the Earth's atmosphere (see for example the review by Quirrenbach in Chapter 5). Two different approaches are widely used to deal with the problem of atmospheric and instrumental phase corruption: closure phase methods (or phase self-calibration), and phase-referencing. In the latter technique, the phase information from a reference object is used to determine the atmospheric phase, and to correct the phase of the target source accordingly. Both methods have been used extensively at radio wavelengths, so one could hope to apply the same techniques in the visible and near-infrared. However, while in radio astronomy the atmospheric coherence time τ_0 is typically several minutes, and the isoplanatic angle θ_0 several degrees, the corresponding values in the optical regime are only of order ten milliseconds and a few arcseconds.

These limitations have important consequences for phase-referencing in the visible and near-infrared. They preclude the use of source-switching strategies and require the simultaneous observation of target and reference object. While this might appear to be a very restrictive requirement, there are several important applications of phase-referencing to optical long-baseline interferometry. First, the phase difference can be used as the primary observable in "astrometric" applications, e.g. to determine the positional offset of a circumstellar envelope from the central star, or to search for the reflex motion of stars orbited by planets. (In the latter case, a suitable reference object is needed within the isoplanatic patch.) Second, the

reference phase can be used to increase the effective atmospheric coherence time, allowing longer coherent integrations on the target source. As we shall see, phase-referencing can improve the sensitivity of large interferometers by many magnitudes; it is therefore a key technique for imaging faint objects. There are different variants of phase referencing: the reference phase can come from simultaneous observations of a separate object (dual-star observations), from observations of the target source with a second wavelength channel (wavelength bootstrapping), or from a more sensitive baseline in an interferometer array (baseline bootstrapping).

9.2 Principles of Phase Referencing

9.2.1 The Mark III Interferometer

We will use a relatively simple instrument, the Mark III interferometer (Shao *et al.* 1988, see Figure 9.1), to explain some the principles of phase referencing. This means that we can concentrate on one specific fringe-tracking technique (explained below), and that we can ignore detector and background noise compared to the photon noise. Our qualitative conclusions remain valid in many more general situations, however, and our quantitative results can easily be generalized for more complex fringe-tracking schemes and more general sources of noise (see e.g. Shao and Colavita 1992).

The Mark III optical interferometer was operational on Mt. Wilson, CA, from 1986 to 1990. Its basic optical layout was that of a single-baseline Michelson interferometer, with two siderostats feeding the two arms, and vacuum delay lines to compensate for the pathlength difference. The baseline of the instrument could be configured to lengths ranging from 3.0 to 31.5 m, giving some flexibility for measurements of stellar diameters and observations of binary stars. The maximum aperture size of the Mark III was 5 cm. The images of stars from both arms of the interferometer were centered by an angle tracker, which worked in the wavelength range $450\,\mathrm{nm} \lesssim \lambda \lesssim 600\,\mathrm{nm}$.

The delay was modulated with a 500-Hz triangle wave of amplitude 800 nm. If the path-length difference between the two interferometer arms was within the coherence length, the intensity at the output of the beam combiner would thus vary sinusoidally with time. The phase of this signal was computed in real time and used to track the movement of the fringes due to atmospheric pathlength fluctuations. The closed-loop bandwidth of the fringe tracker was $\sim 20\,\mathrm{Hz}$. Under favorable seeing conditions, the fringes stayed locked for several seconds, sometimes up to a few minutes. Once per second, the fringe amplitude was compared to a preset value. If it was lower than this threshold, the fringe tracker assumed that it was not locked on the central fringe and jumped one fringe; the direction was determined by the visibility gradient.

Dichroic beam splitters in the two output arms of the beam combiner provided four spectral channels. A broad-band channel ($600\,\mathrm{nm} \lesssim \lambda \lesssim 900\,\mathrm{nm}$, giving an effective fringe-tracking

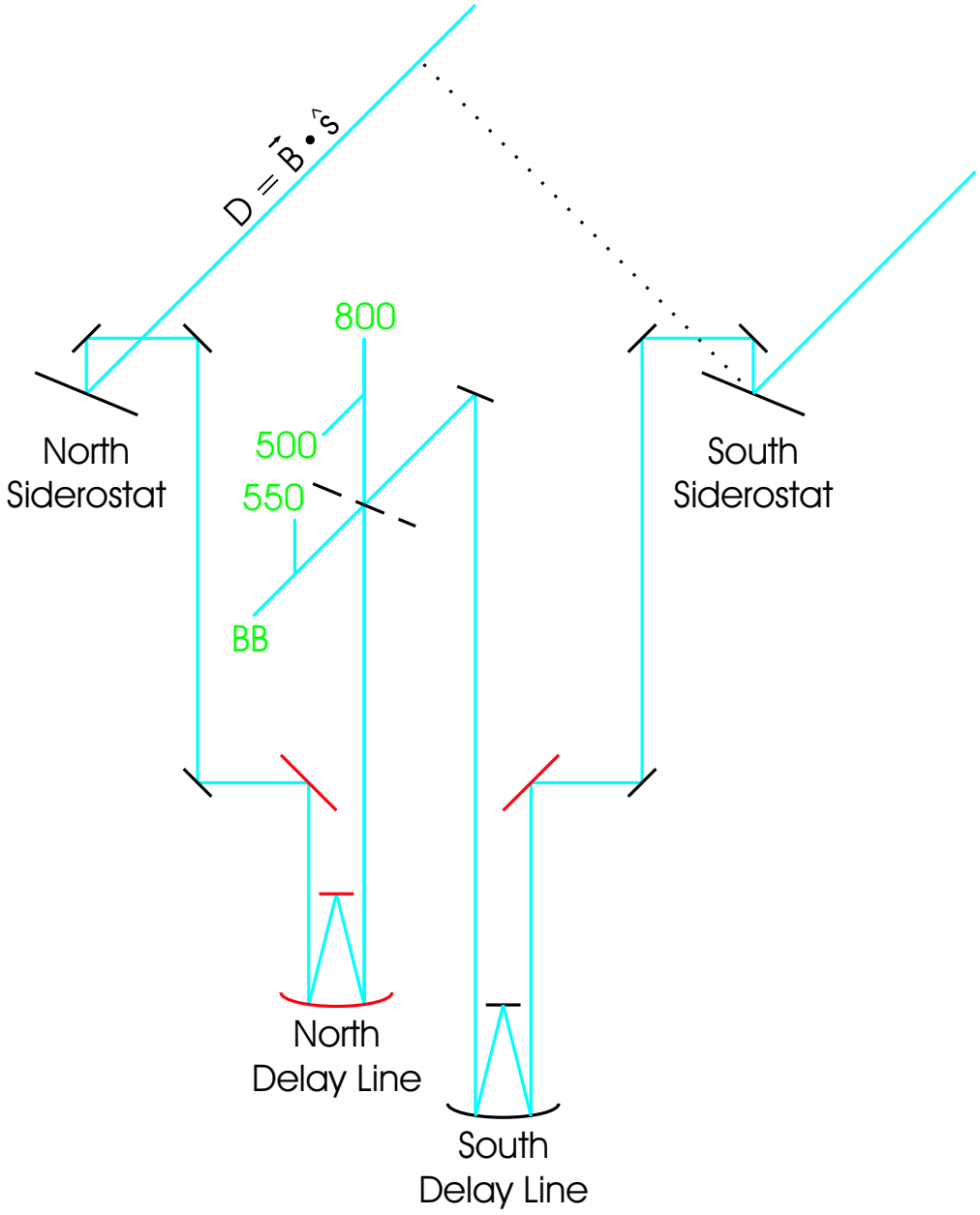

Figure 9.1: Schematic drawing of the Mark III interferometer. The two siderostats feed light into a vacuum system. The two mirrors feeding light into the delay lines are mounted on piezo-electric actuators and are part of the angle-tracking servo loop. The positions of the two optical delay lines are continuously monitored with a laser interferometer. They are optically equivalent, but the cart and the small mirror in one of them are actively controlled and are part of the fringe-tracking servo loop. The beams from the two arms are combined with a 50% reflective mirror. The light in each of the two outputs is divided with a dichroic beam splitter, so that four wavelength channels (broad band for fringe tracking, 500 nm, 550 nm, and 800 nm in the standard setup) are available.

wavelength $\lambda_t \simeq 700\,\mathrm{nm}$) was used to track the fringes, while substantially narrower bandpasses defined by interference filters were used in the other channels to take the scientific data. This arrangement ensured that the fringe packet was much wider in the data channels than in the tracking channel, so that errors in the central fringe identification did not lead to a noticeable visibility reduction.

9.2.2 Visibility Estimation and Signal-to-Noise Ratio

For each of the four spectral channels, arriving photons are counted synchronously with the delay modulation in bins corresponding to $\lambda/4$. (Since the physical stroke is equal to λ only in the channel with the longest wavelength, dead time is added in the electronics at the end of the stroke in the other three channels.) From the four bin counts A, B, C, and D, the square of the visibility V^2 can be estimated using

$$V^2 = \frac{\pi^2}{2} \cdot \frac{\langle X^2 + Y^2 - N \rangle}{\langle N - N_{\mathrm{dark}} \rangle^2} \quad , \tag{9.1}$$

where $X = C - A$ and $Y = D - B$ are the real and imaginary parts of the visibility, $N = A + B + C + D$ is the total number of photons counted, and N_{dark} is the background count rate determined separately on blank sky. This estimator for V^2 is not biased by photon noise (Shao *et al.*, 1988). The visibility phase is estimated using

$$\phi = \arctan\left(\frac{Y}{X}\right) - \frac{\pi}{4} \quad . \tag{9.2}$$

The data are averaged using a combination of coherent and incoherent integrations.* By choosing a coherent integration time T, an observation of total duration $M \cdot T$ is divided into M intervals, which are averaged incoherently. The variance of the V^2-estimator (Equation 9.1) is then given by

$$\sigma^2 = \frac{\pi^4}{4MN^2} + \frac{\pi^2 V^2}{MN} \quad , \tag{9.3}$$

where N is the number of photons detected per coherent integration time (Colavita, 1985). The signal-to-noise ratio (SNR) of V^2 is therefore

$$\mathrm{SNR}(V^2) = \frac{2}{\pi^2} \cdot \frac{\sqrt{M} N V^2}{\sqrt{1 + \frac{4}{\pi^2} N V^2}} \quad . \tag{9.4}$$

If $NV^2 \gg 1$, the second term in Equation 9.3 dominates, and the variance depends only on the total number of photons detected, MN. If however $NV^2 \ll 1$, the first term is the dominant one, and the variance for a given total duration of the observation (i.e.,

*Coherent integration means that we sort each photon arriving during the integration time in one of the bins A, B, C, D, and use Equation 9.1 to get an estimate of V^2. Incoherent integration means that we average over many estimates of V^2. The intuitive meaning is that the coherent integration is used to estimate both amplitude *and phase* of the visibility, whereas the incoherent integration averages over the *modulus* of the visibility.

constant total number of photons MN) decreases with increasing coherent integration time, $\sigma^2 \propto N^{-1} \propto T^{-1}$; this implies that the signal-to-noise ratio of V^2 is $\propto T^{1/2}$ (for constant $M \cdot T$). We will call the two cases the "photon-rich" and "photon-starved" regimes, although NV^2, and not N, is the critical quantity.

The extremely important results captured in Equations 9.3 and 9.4 have a simple intuitive interpretation. If the coherent integration time is sufficiently long, we get a good estimate of the amplitude *and phase* of the complex visibility. We can then stop the coherent integration, write out V^2 for a data sample, and average over these samples later without losing sensitivity. This is the photon-rich regime. If we are forced to stop the coherent integration (e.g., because of variations in the atmospheric or instrumental phase) before we get a meaningful phase measurement, we can still estimate V^2 for each data sample, but averaging over these estimates gives the poorer signal-to-noise characteristic of the photon-starved regime.

While these considerations show that it is advantageous to choose T large enough to get into the photon-rich regime, values larger than a fraction of the atmospheric coherence time will lead to serious phase changes and therefore to unacceptable degradation of the visibility. In the Mark III "standard" data reduction for measurements of stellar diameters and binary stars, $T = 4\,\mathrm{ms}$ is adopted, which gives a coherence loss of a few per cent for seeing conditions typical for Mt. Wilson.

Several calibrator stars are normally included in the observing list for each night. They are used to determine the "system visibility" V^2_{sys}, i.e., the value of V^2 observed for unresolved stars, as a function of seeing, zenith angle, time, and angle of incidence on the siderostat mirrors. For the seeing calibration, a seeing index S is calculated for each observation from the residual delay (Mozurkewich *et al.*, 1991). After removing the relatively strong dependence of V^2 on S, calibration with respect to the other variables normally leads to only a slight further improvement. (This situation is changed for phase-referenced data, where an additional strong decrease of V^2 with zenith angle has to be taken into account, see Section 9.3.8). The raw values of V^2 determined from Equation 9.1 are then divided by V^2_{sys} to obtain calibrated data V^2_{cal} for further analysis. Both the internal noise, with contributions from photon noise and from short-term fluctuations, and the calibration uncertainty contribute to the error of V^2_{cal}. The two terms are added in quadrature to obtain formal error bars.

9.2.3 Phase-Referenced Visibility Averaging

The wide-band tracking channel in the Mark III interferometer provides a phase reference, which can be used to extend the coherent integration time T beyond the limit imposed by the atmospheric turbulence. This method provides a means of obtaining substantially

better signal-to-noise in the photon-starved regime, or even to make a transition into the photon-rich regime. The phase-referenced quantities X_r, Y_r, V_r, and ϕ_r are defined by

$$X_r + iY_r = V_r\,\mathrm{e}^{i\phi_r} = V_s\,\mathrm{e}^{i(\phi_s - \frac{\lambda_t}{\lambda_s}\phi_t)} \quad , \tag{9.5}$$

where λ_s, V_s, ϕ_s are the wavelength, visibility, and phase in the signal channel, and λ_t, ϕ_t the wavelength and phase in the tracking channel. In practice, V_r^2 is computed from Equation 9.1 using X_r and Y_r instead of X and Y; this procedure retains the advantage of using an unbiased estimator.

Equation 9.5 assumes that the atmospheric phase at λ_s is given by $(\lambda_t/\lambda_s)\phi_t$. If this were the case exactly, there would be no coherence losses, and the integration time could be arbitrarily long. A number of systematic effects (discussed in more detail in Section 9.3, see also Quirrenbach *et al.* 1994) can lead to a decorrelation of the phases between the signal and tracking channels, however. They introduce additional phase noise, which reduces the system visibility and limits the maximum integration time. The dependence of the system visibility on seeing and zenith angle is also made steeper, which increases the uncertainty of the calibration. In practice, therefore, phase-referenced averaging involves trading off some calibration accuracy for the gain in signal-to-noise.

9.2.4 Limb Darkening of Arcturus

A good example for the use of phase-referenced visibility averaging are the Mark III observations of limb darkening in Arcturus (Quirrenbach *et al.*, 1996). The main challenge of limb-darkening measurements is the need to collect data in the vicinity of and beyond the first zero of the visibility function.[†] The signal-to-noise ratio (Equation 9.4) of these measurements is normally very small. Since $V^2 \ll 1$, even observations of extremely bright stars like Arcturus may be in the "photon-starved" regime, and phase-referencing may lead to a substantial improvement. Fortunately the fringe-tracking channel of the Mark III interferometer provides a convenient phase reference. The signal-to-noise ratio in this channel is much higher than in the 550 nm signal channel, first because the tracking channel has a much larger bandwidth, and second because the tracking wavelength is longer and therefore has a higher visibility (see also Figure 9.4).

Figure 9.2 shows Mark III visibility measurements for Arcturus at 550 nm. The three baselines were chosen to bracket the first zero of the visibility function at that wavelength. The data were processed with phase-referencing (Equation 9.5), and a coherent integration time of 256 ms was chosen. The 3σ upper limit for the smallest visibilities plotted in Figure 9.2 is $V^2 \leq 10^{-4}$. This means that the data close to the zero would be in the photon-starved regime for the "standard" Mark III coherent integration time of 4 ms; the error bars would be much larger with the standard processing. The effect of varying the coherent integration time is illustrated in Figure 9.3. In this figure, the formal error of V^2

[†]On short baselines the visibility function of a limb-darkened disk is virtually indistinguishable from that of a somewhat smaller uniform disk.

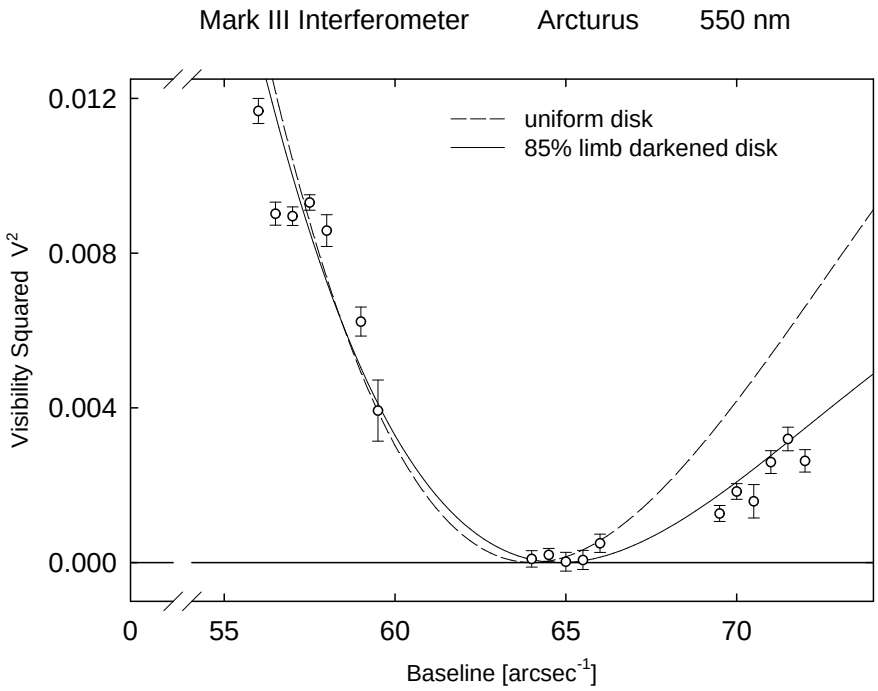

Figure 9.2: Mark III visibility data on α Boo (Arcturus) at $\lambda_s = 550$ nm on three different baselines near the first zero of the visibility function. The data were processed with the phase-referenced averaging algorithm, using a coherent integration time of 256 ms.

is plotted versus V^2 for a number of observations very close to the zero of the visibility function. Each observation was processed with four different coherent integration times (4 ms, 32 ms, 256 ms, and 1024 ms). We see that with increasing integration time both the formal errors (vertical position of the data points in Figure 9.3), as well as the scatter between them (horizontal spread of the points) get smaller. The dashed lines correspond to a -1σ-deviation from $V^2_{\rm cal} = 0$, and a $+1\sigma$-deviation from $V^2_{\rm cal} = 2 \cdot 10^{-4}$. It can be seen from the figure that almost all data points are consistent with $0 \leq V^2_{\rm cal} \leq 2 \cdot 10^{-4}$ on the 1σ level, but the uncertainty of the V^2cal estimate gets much smaller with increasing coherent integration time.

9.2.5 Further Applications of Same-Source Phase Referencing

The Mark III observations of Arcturus described in the previous section are an example of *wavelength bootstrapping*. This technique uses the fact that the signal-to-noise ratio may be high at a certain wavelength λ_1, but low at another wavelength λ_2. An important case, illustrated in Figure 9.4, is the situation where the difference in signal-to-noise is due to V^2 being high at λ_1, but low at λ_2. It is then possible to observe at λ_2, while the fringe tracker is working at λ_1. For example, wavelength bootstrapping is useful for imaging stellar photospheres, where λ_1 can be in the IR and λ_2 in the visible, or for imaging circumstellar

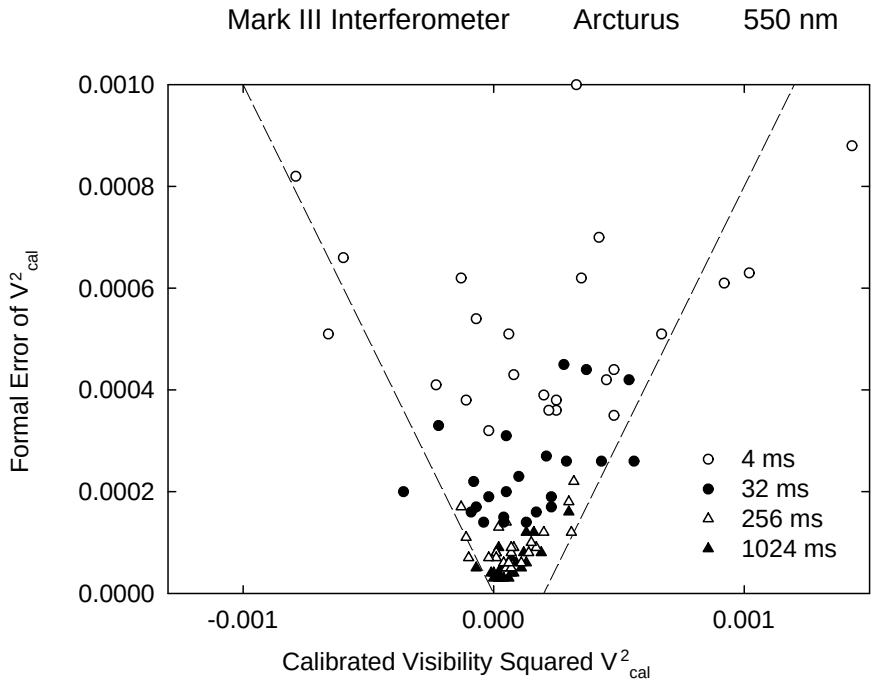

Figure 9.3: Mark III data on α Boo (Arcturus) at 550 nm, very close to the first zero of the visibility function (corresponding to the group of points near 65 arcsec^{-1} in Figure 9.2). The plot shows the formal error of $V^2_{\rm cal}$ as a function of $V^2_{\rm cal}$, for four different coherent integration times. All points that are compatible with $0 \leq V^2_{\rm cal} \leq 2 \cdot 10^{-4}$ to within 1σ lie in the wedge-shaped region between the two dashed lines.

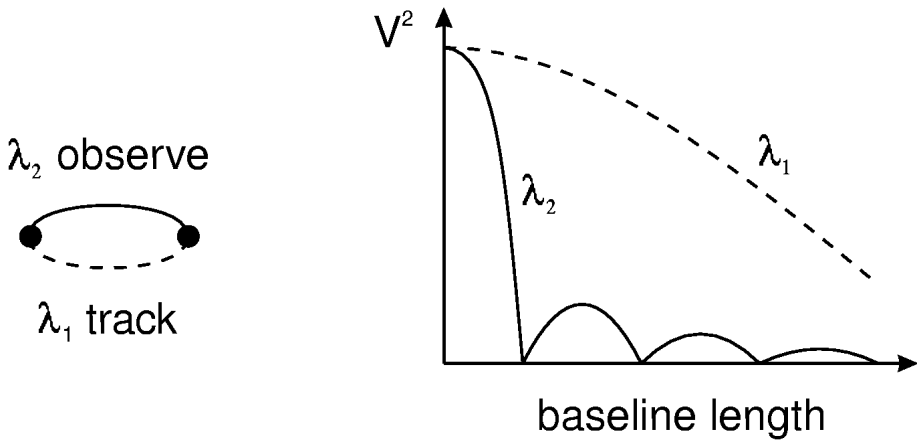

Figure 9.4: Wavelength bootstrapping. The fringes are tracked at a long wavelength. The observations are done on the same baseline, but at a shorter wavelength, where the resolution is higher, but V^2 much smaller.

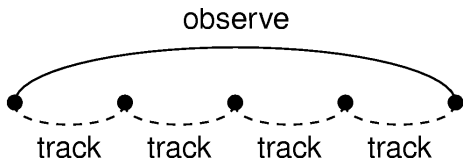

Figure 9.5: Baseline bootstrapping. The fringes are tracked on the short baselines of the array (in this case a five-element linear configuration), where V^2 is high. The observations can then be done on the long baselines.

matter, where λ_1 can be in the continuum (where the small stellar photosphere dominates) and λ_2 in a line emitted by the extended material.

In interferometer arrays with more than two telescopes, a different variant of phase referencing is possible: baseline bootstrapping (see Figure 9.5) uses the signal on the short baselines of the array for the fringe-tracking servo, while data are taken on the long baselines, where V^2 can be much lower.[‡] The configuration of the Navy Prototype Optical Interferometer, which is optimized for observations of stellar surface structure, has been laid out specifically to make use of baseline bootstrapping (Mozurkewich and Armstrong, 1992). A related idea has been developed for arrays with telescopes of different sizes, such as the VLTI and the Keck Interferometer. Fringe tracking is required only on the more sensitive baselines which involve at least one large telescope, while bootstrapping enables observations on the baselines between two small telescopes. It is also possible, of course, to combine baseline bootstrapping and wavelength bootstrapping.

So far we have discussed applications of phase-referencing that use the phase relation between the reference channel and the signal channel only implicitly, to remove the atmospheric phase and to increase the interferometric sensitivity. One can also make explicit use of the referenced phases and use them for *phase-referenced imaging* or *phase-referenced spectroscopy*. If the reference star can be considered a point source (or if its structure phase can be computed and subtracted from the reference phase), the referenced phase can be used directly as the Fourier phase in an image reconstruction algorithm. An example is emission-line observations of circumstellar matter. In many cases the continuum emission of the stellar photosphere provides a nearly point-like reference for the much more extended line emission. The phase difference between line and continuum is then an observable that can be used for imaging the line emission. If sufficient spectral resolution is available, this can even be done separately for a number of radial velocity channels. By referencing to the continuum phase, these channel maps can be registered with respect to each other and with respect to the continuum. One should note that true imaging with full phase information is possible in this way even with a single-baseline instrument (if data are collected succes-

[‡]Clearly, when the pathlength from telescope 1 is kept equal to the pathlength from telescope 2, and the pathlength from telescope 2 equal to that from telescope 3, the paths from telescopes 1 and 3 are also equal. However, one has to keep in mind that the phase errors accumulate along the chain of baselines that are co-phased in this manner.

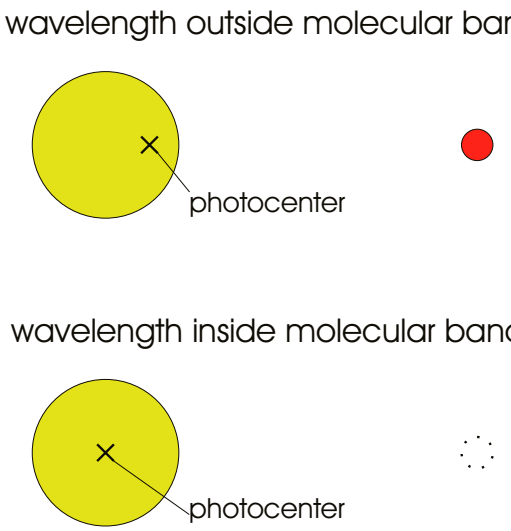

Figure 9.6: The shift of the star – planet photocenter with wavelength gives rise to an interferometric phase shift that can be exploited to obtain a spectrum of the planet.

sively on a sufficient number of points in the (u, v) plane to satisfy the Nyquist sampling theorem).

Another potential application of phase-referencing is the spectroscopy of faint stellar companions (Quirrenbach, 2000). For example, the near-infrared spectra of extrasolar planets should be characterized by extremely deep absorption bands of water and methane. The photocenter of a star-planet system is therefore slightly different outside the molecular bands, where the planet is relatively bright, and within the bands, where it is much dimmer (see Figure 9.6). The shift of the photocenter is proportional to the planet / star brightness ratio and can thus be used as a proxy for the planet spectrum. The shift of the photocenter gives rise to a corresponding wavelength dependence of the interferometer phase, which can be measured if the signal-to-noise ratio is sufficient and systematic effects are kept small. In the case of "hot Jupiters," which are quite favorable because the planets are close to their parent stars and therefore hot and bright, the expected effect on the interferometer phase is ~ 0.5 mrad on the longest baselines of the Keck Interferometer or VLTI. This could be measured with a signal-to-noise ratio of ~ 3000, but reducing the systematic instrumental and atmospheric effects to that level will be a very challenging task.

9.2.6 Off-Source Phase Referencing

A common characteristic of the techniques discussed so far is that the reference phase is measured on the target object itself, either at a different wavelength or on a different baseline. This helps for observations of bright objects in the low-visibility (and therefore "photon-starved") regime, and for specific spectroscopic applications. For faint objects, however, one would clearly like to emulate the phase calibration procedure widely used in radio astronomy in which the atmospheric phase is determined from a bright source near the

target. In radio interferometry one can slew the telescope between target and reference in intervals of several minutes, but because of the short atmospheric coherence time at visible and near-infrared wavelengths, here the target and the reference have to be observed truly simultaneously. Off-source fringe tracking is therefore possible only in interferometers with a field much wider than feasible in a Michelson instrument; either a wide-field (e.g., Fizeau) setup or a *dual-star system* is required. In a dual-star interferometer, each telescope accepts two small fields and sends two separate beams through the delay lines. The delay difference between the two fields is taken out with an additional short-stroke differential delay line; an internal laser metrology system is used to monitor the delay difference (which is equal to the phase difference multiplied with $\lambda/2\pi$, of course). Dual-star interferometry has been demonstrated by the Palomar Testbed Interferometer (Colavita *et al.*, 1999); it is a vital component of the plans for the Keck Interferometer (Colavita *et al.*, 1998) and the VLT Interferometer (Quirrenbach *et al.*, 1998).

The dual-star technique has been developed mainly for interferometric astrometry (another application of phase referencing that makes explicit use of the phase difference), but it can also be used for phase-referenced visibility averaging or phase-referenced imaging. The most important problem encountered by all off-source phase-referencing techniques is anisoplanatism, i.e., the fact that atmospheric fluctuations are only partly correlated in different sky directions (see Section 9.3.7 below). The phase noise associated with anisoplanatism causes astrometric errors, and reduces the phase-referenced visibility dramatically if the distance to the reference source exceeds the isoplanatic angle. The need to find a reference object within the isoplanatic patch is a severe limitation for off-source phase-referencing; the chances to find a suitably bright star for a randomly chosen target are typically one in a hundred or worse. Still, there are a number of important astrophysical applications for this technique: astrometric searches for unseen companions (e.g., planets)[§], observations in clusters (e.g., near the Galactic Center), and programs in which a few suitable targets can be drawn from comparatively long lists (e.g., observations of extragalactic sources that happen to be close in the sky to a bright star).

The reference source can also be used for adaptive optics wavefront sensing, if such a system is available. In this case the whole entrance pupil of the interferometer is made fully cophased and the sensitivity of the interferometer is essentially identical to the sensitivity of a single telescope with the same diameter. It is thus important to realize that *bright objects are needed to cophase an interferometer, but very faint sources can be observed in a limited field around these reference sources.*

[§]In this case the target is normally a nearby and therefore bright star, which can be used for fringe tracking. It is still necessary to find nearby astrometric reference stars, but they can be much fainter, because phase-referenced fringe tracking can be applied to them: the *astrometric target* is the *interferometric reference* for the astrometric reference stars.

9.3 Phase Decorrelation Mechanisms

9.3.1 Phase Errors and Coherence Losses

We will now discuss a number of mechanisms that lead to phase errors and therefore to coherence losses and to a reduction of the phase-referenced visibility. These effects can be broadly divided into two classes, namely those mechanisms that are due to errors in the determination of the phase in the reference channel (Sections 9.3.2–9.3.5), and those that are due to atmospheric propagation effects (Sections 9.3.6–9.3.9). While some of the former processes are instrument-dependent and can be reduced (or even avoided) by improved interferometer and fringe-detector designs, the latter class sets fundamental limits to the application of phase-referencing methods from the ground. We will again use phase-referenced visibility averaging with the Mark III interferometer to give some specific numerical examples (see also Quirrenbach *et al.* 1994).

If the variance of the referenced phase ϕ_r associated with a decorrelation mechanism is $\sigma^2_{\phi,r}$, it will reduce V_r^2 by a factor η, which can be computed from

$$\eta = \mathrm{e}^{-\sigma^2_{\phi,r}} \quad . \tag{9.6}$$

For assessing the individual mechanisms, it is not only important to compare the numerical values of the associated phase variances, but also to note their dependencies on observing conditions (e.g. seeing, zenith angle) and particularly on stellar parameters (e.g. colors). While the standard calibration procedure will correct for a uniform reduction of V^2, and to some extent for variations with observing conditions, effects that differ from star to star can introduce systematic errors that are difficult to detect. A priori limits on these effects are therefore necessary for practical applications of phase-referenced visibility averaging.

9.3.2 Photon Noise in the Tracking Channel

The finite number of photons detected during each coherent integration interval (4 ms in the Mark III case) sets a fundamental limit to the precision of the reference phase determination. The variance of ϕ_r due to photon noise in the tracking channel is

$$\sigma^2_{\phi,r} = \left(\frac{\lambda_t}{\lambda_s}\right)^2 \sigma^2_{\phi,t,\mathrm{phot}} = \left(\frac{\lambda_t}{\lambda_s}\right)^2 \cdot \frac{2}{N_t V_t^2} \quad , \tag{9.7}$$

where N_t and V_t are the number of the photons counted and the visibility in the tracking channel. $\sigma^2_{\phi,r}$ depends on the brightness and color of the star, and even on the baseline length (through V_t^2). However, for the fringe tracker to work reliably under average seeing conditions, $N_t V_t^2 \simeq 70$ is needed for the 4 ms sampling interval, giving $\eta \simeq 0.98$ for $\lambda_t = 700\,\mathrm{nm}$, $\lambda_s = 800\,\mathrm{nm}$, and $\eta \simeq 0.95$ for $\lambda_t = 700\,\mathrm{nm}$, $\lambda_s = 500\,\mathrm{nm}$. Thus the visibility reduction is slight even for stars that are close to the sensitivity limit of the fringe tracker, and negligible for stars that are substantially brighter. It is also possible to introduce the signal-to-noise in the tracking channel as an additional independent variable in the calibration process, if very high accuracy is required.

9.3.3 Color and Visibility Dependence of the Effective Tracking Wavelength

To achieve high sensitivity (and to keep the errors due to photon noise small), the bandpass in the fringe-tracking channel should be made as wide as possible. The effective wavelength to be used in Equation 9.5 is then given by

$$\lambda_t = \frac{\int d\lambda\, \lambda\, W_t(\lambda) N(\lambda) V(\lambda)}{\int d\lambda\, W_t(\lambda) N(\lambda) V(\lambda)} \quad , \tag{9.8}$$

where $N(\lambda)$ is the number of photons emitted by a star as a function of wavelength, $V(\lambda)$ the visibility, and $W_t(\lambda)$ the combined response of atmosphere, instrument, and detector. If the wavelength used in Equation 9.5 differs from the true effective wavelength by $\delta\lambda_t$, the resultant variance of the reference phase is

$$\sigma^2_{\phi,r} = \left(\frac{\delta\lambda_t}{\lambda_s}\right)^2 \cdot \langle\phi_t^2\rangle \quad . \tag{9.9}$$

As evident from Equation 9.8, the true effective wavelength depends on stellar colors and diameters, and on the baseline length. If for simplicity one uses $\lambda_t = 700\,\mathrm{nm}$ for all stars, $\delta\lambda_t \lesssim 25\,\mathrm{nm}$ for the parameters of the Mark III interferometer. With the additional assumption that the residual atmospheric phase rms not tracked by the fringe tracker $\sqrt{\langle\phi_t^2\rangle} \lesssim 2\,\mathrm{rad}$, $\eta \gtrsim 0.99$ is derived from Equation 9.9.

9.3.4 Stroke Mismatch

In pathlength modulation schemes like that used by the Mark III, any difference between the stroke of the 500 Hz pathlength modulation and the wavelength λ will also lead to errors in the phase estimation, since then the bins A, B, C, and D do not correspond exactly to $\lambda/4$. (This correspondence is assumed implicitly in Equation 9.2.) For each channel, the gating of the electronic counters for A, B, C, and D has to be set by the on-line control system to match one quarter of the nominal wavelength. In this way, an effective stroke s is created for each channel. Defining

$$\varepsilon = \frac{2\pi}{\lambda} \cdot (s - \lambda) \quad \text{and} \quad \delta = \frac{\cos\varepsilon/4}{1 + \sin\varepsilon/4} \quad , \tag{9.10}$$

it has been shown by Colavita (1985) that

$$\tan\phi_{\mathrm{est}} = \delta \cdot \tan\phi_{\mathrm{true}} \quad , \tag{9.11}$$

where ϕ_{est} is the phase estimated from Equation 9.2, and ϕ_{true} is the true phase. For a complete treatment of the effect of the stroke mismatch, these equations have to be integrated over λ, with a suitable weighting function representing the bandpass of the tracking channel. To first order, however, it can be assumed that the phase error is given by Equations 9.10 and 9.11, evaluated at $\lambda = \lambda_t$. For $s_t - \lambda_t \leq 25\,\mathrm{nm}$, a phase error $\phi_{\mathrm{est}} - \phi_{\mathrm{true}} \leq 2^\circ$ is then obtained. Errors of this order can be safely ignored for most visibility averaging applications, but may be important for phase-referenced imaging and spectroscopy.

9.3.5 Fringe Jumps

An ideal fringe tracker would follow the atmospheric pathlength fluctuations to a fraction of λ_t, and ϕ_t would always be well within the interval $(-\pi, \pi)$. In practice, however, temporary excursions from the central fringe that are larger than $\lambda/2$ may occur, and the phase has to be "unwrapped" by the phase-referencing algorithm. This is done by imposing the requirement that the phase in successive data segments (4 ms intervals for the Mark III) should be continuous. While this process normally works well, occasional misidentifications are possible. It is obvious from Equation 9.5 that a 360° error in ϕ_t will lead to a phase jump in ϕ_r.

If the average number of these jumps during the coherent integration time T is small, the coherence loss is not dramatic. This requirement sets an upper limit to T. Since the probability of unwrapping errors depends only on the seeing and on the signal-to-noise in the tracking channel, it can be accounted for in the calibration procedure. In a series of tests with the Mark III, it turned out that the degradation of the phase-referenced visibility V_r due to fringe jumps was not serious for integration times up to 2 s, for average seeing conditions on Mt. Wilson.

9.3.6 Dispersion

While Equation 9.5 assumes that the atmospheric pathlength fluctuations are independent of wavelength, they are actually larger in the blue spectral range than in the red, because of dispersion. The two-color dispersion coefficient D is defined by

$$D = \frac{n(\lambda_t) - 1}{n(\lambda_s) - n(\lambda_t)} \quad , \tag{9.12}$$

where $n(\lambda)$ is the refractive index of air at λ. Typical values for $\lambda_t = 700\,\mathrm{nm}$ and $\lambda_s = 450$, 500, 550, and 800 nm are $D = 59$, 87, 137, and -364, respectively. If the total "unwrapped" phase in the tracking channel is denoted Φ_t, a phase error $(\lambda_t/\lambda_s)(\Phi_t/D)$ is introduced by the dispersion. Since the largest phase excursions occur on long time scales, this sets a limit to the coherence time. For Kolmogorov turbulence, the coherence time $t_{0,r}$ of ϕ_r is given by

$$t_{0,r} = |D|^{6/5}\, t_{0,s} \quad , \tag{9.13}$$

where $t_{0,s}$ is the atmospheric coherence time in the data channel (Colavita, 1992). Under average conditions on Mt. Wilson, $t_{0,s}$ is of order 6 to 8 ms at 500 nm. For integration times up to about 2 s, the coherence losses due to dispersion are therefore tolerable for visibility averaging, and they can be taken into account by the calibration procedure.

It is obviously possible to deal with dispersion explicitly by using

$$\tilde{\phi_r} = \phi_s - \frac{\lambda_t}{\lambda_s}\phi_t - \frac{\lambda_t}{\lambda_s} \cdot \frac{\Phi_t}{D} \tag{9.14}$$

instead of ϕ_r as defined in Equation 9.5. While this approach can reduce the phase errors by a factor ~ 10, a residual effect due to water vapor fluctuations remains, because their dispersion is different from the values applicable to dry air.

9.3.7 Anisoplanatism

If the reference phase is measured on a star at an angular separation θ from the target object, there will be some decorrelation because the light from the two sources passes through different turbulence cells. The angle θ_i for which the variance of the relative phase is $1\,\mathrm{rad}^2$ is called the isoplanatic angle. In interferometric applications, the independent contributions from the two arms of the interferometer have to be taken into account, giving a somewhat smaller value for θ_i. Under the assumption of a Kolmogorov turbulence spectrum with refractive index structure constant $C_n^2(h)$ at height h, the interferometric isoplanatic angle is

$$\theta_i = \left[5.82\,k^2(\sec z)^{8/3}\int_0^\infty dh\,C_n^2(h)h^{5/3}\right]^{-3/5} \quad , \tag{9.15}$$

where $k = 2\pi/\lambda$ is the wavenumber (assumed here to be equal for the target and reference channels), and z the zenith angle. While this expression holds for small apertures, a somewhat more optimistic estimate is obtained for larger apertures (Colavita, 1992). Typical values for θ_i are of order a few arcseconds, much larger than the interferometric field of view of a Michelson interferometer. In applications where the reference phase is measured on the object of scientific interest itself, anisoplanatism does not occur at all. However, it is the most severe limitation for dual-star interferometry. We see from Equation 9.15 that $\theta_i \propto k^{-6/5} \propto \lambda^{6/5}$; this means that finding reference stars for dual-star interferometry is much easier at longer wavelengths.

9.3.8 Differential Refraction

An effect somewhat similar to anisoplanatism occurs even when the angular separation between the target and the reference is zero. If $\lambda_s \neq \lambda_t$, the beams at the two wavelengths follow different paths through the atmosphere at non-zero zenith angles, due to differential refraction. For a Kolmogorov turbulence spectrum, the corresponding phase variance is

$$\sigma^2_{\phi,r} = 5.82\,k_s^2\left[\frac{h_0\,(n(\lambda_t)-1)\,\mathrm{e}^{-h_1/h_0}}{D}\right]^{5/3}\tan^{5/3}z\,\sec^{8/3}z\int_0^\infty dh\,C_n^2(h)\left(1-\mathrm{e}^{-h/h_0}\right)^{5/3} \quad , \tag{9.16}$$

where $k_s = 2\pi/\lambda_s$ is the wavenumber in the signal channel, $n(\lambda_t)$ is the atmospheric index of refraction at λ_t, D is the atmospheric dispersion between λ_s and λ_t defined by Equation 9.12, h_0 is the scale height of the atmospheric density, h_1 is the elevation of the observatory site above sea level, z is the zenith angle, and $C_n^2(h)$ is the refractive index structure constant. Again, this estimate might be somewhat pessimistic, since averaging over the aperture has not been taken into account.

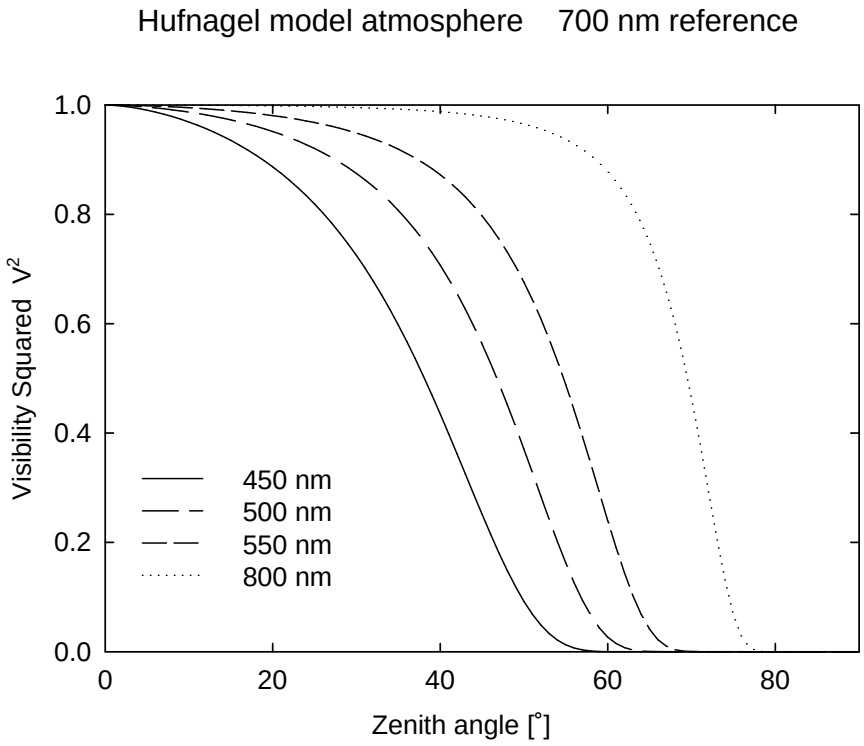

Figure 9.7: Reduction of V^2 due to differential refraction as a function of zenith angle z, predicted from a Hufnagel (1974) model atmosphere. The reference wavelength $\lambda_t = 700\,\mathrm{nm}$; the wavelength in the data channels $\lambda_s = 450$, 500, 550, and 800 nm.

The phase variance due to differential refraction depends very strongly on z; while it is negligible close to the zenith, it is the dominant decorrelation mechanism at intermediate to large zenith angles for the parameters of the Mark III phase-referenced visibility averaging experiments. From Equation 9.16 it is obvious that differential refraction—like anisoplanatism—is more strongly affected by high-altitude turbulence than by disturbances close to the ground. This is expected, since the beams from target and reference coincide at the telescope aperture; their separation increases with height when they are traced back through the atmosphere. To carry out quantitative calculations of differential refraction, it is therefore necessary to know the turbulence profile; in the absence of better measurements we use the model for the atmospheric turbulence as a function of height h (in m) by Hufnagel (1974),

$$C_n^2(h) = 2.7 \cdot \left(2.2 \cdot 10^{-53} h^{10} \mathrm{e}^{-h/1000} + 10^{-16} \mathrm{e}^{-h/1500}\right) \quad . \tag{9.17}$$

Figure 9.7 shows the reduction of V_r^2 derived from a numerical integration of Equation 9.16, with the Hufnagel turbulence profile. The values $h_0 = 8\,300\,\mathrm{m}$, $h_1 = 1\,700\,\mathrm{m}$ (applicable to Mt. Wilson), $\lambda_t = 700\,\mathrm{nm}$, and $\lambda_s = 450$, 500, 550, and 800 nm were used. This figure demonstrates that differential refraction leads to a much steeper dependence of the system visibility with zenith angle in the phase-referenced data than in incoherent averages. This

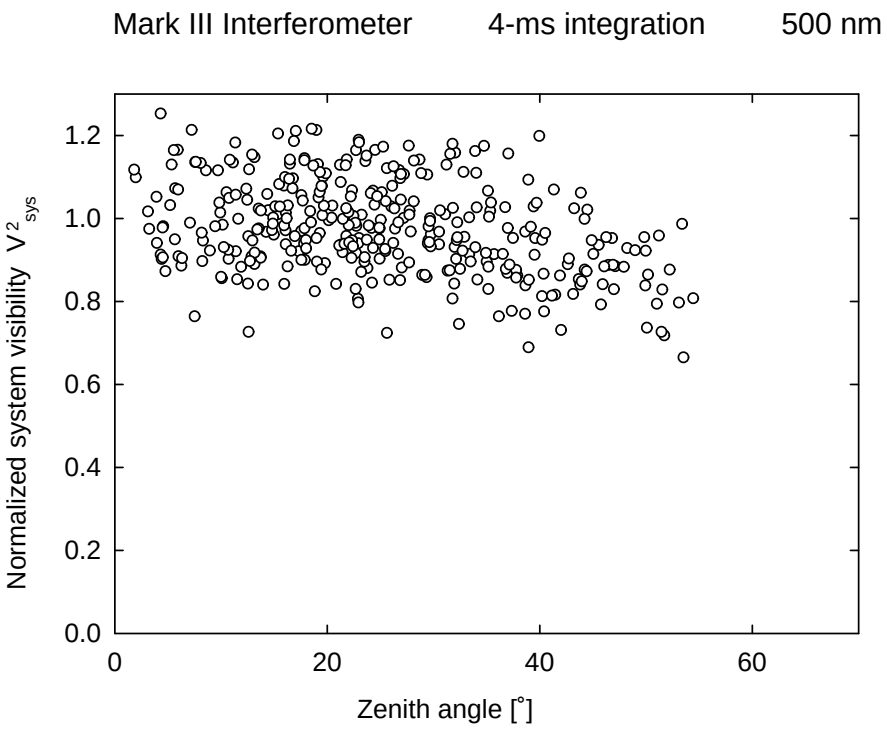

Figure 9.8: Observed V^2 divided by an estimate $V^2_{\rm est}$ from photometric data, for 16 stars at 500 nm. The data were obtained on the nights July 29 and July 31, 1989; they are plotted a function of zenith angle z. Each night was normalized to 1 at $z = 0$. Each measurement corresponds to one 75-s observation. The standard data reduction procedure was used, which averages the 4-ms samples incoherently.

effect is particularly important in the blue spectral range, where the dispersion is large (small values of D). Differential refraction therefore restricts the application of phase-referenced visibility averaging to moderate zenith angles, depending on the wavelength λ_s and on the seeing.

Figure 9.8 shows the Mark III system visibility for two nights (July 29 and 31, 1989) as a function of zenith angle z, for the data integrated incoherently with the standard method; it has been normalized to $V^2_{\rm sys} = 1$ at $z = 0$. It is obvious that $V^2_{\rm sys}$ varies only slightly with z; this variation is mostly due to the degradation of the seeing for longer pathlengths through the atmosphere. Figure 9.9 shows the same data, but processed with the phase-referencing algorithm, using an integration time of 1024 ms. A strong reduction of the system visibility is now apparent at $z \gtrsim 40°$. The solid line indicates the visibility reduction due to differential refraction predicted by the Hufnagel (1974) atmosphere model. The qualitative agreement between the observations and this model demonstrates that differential refraction is indeed the dominant reason for coherence losses at intermediate to large zenith angles.

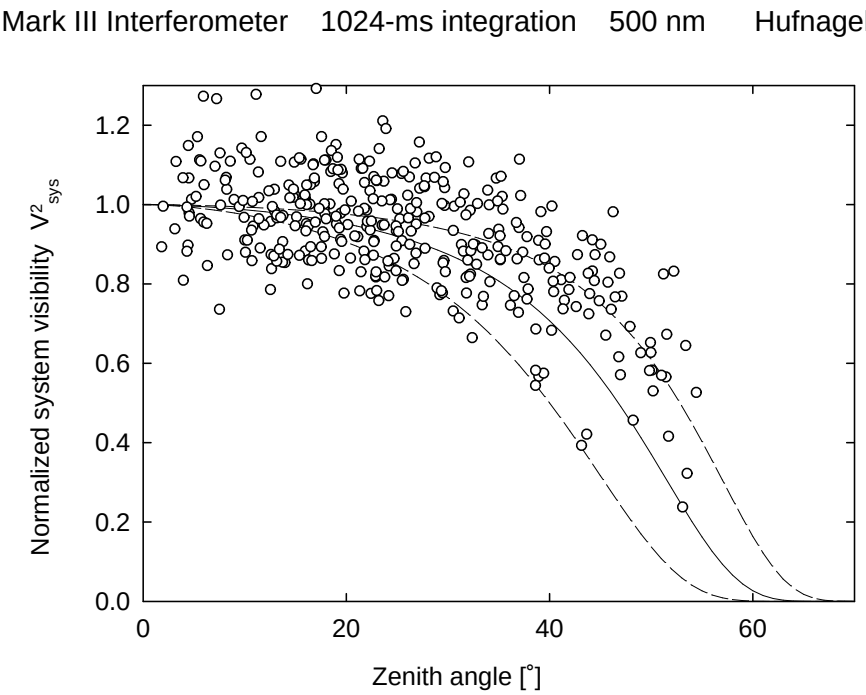

Figure 9.9: The same data as in Figure 9.8, but processed with the phase-referenced averaging algorithm. The coherent (phase-referenced) integration time is 1024 ms. The solid curve is the visibility reduction due to differential refraction predicted by the Hufnagel model atmosphere; the dashed curves correspond to atmospheres that have 0.5 and 2 times the C_n^2 of the Hufnagel model at all heights.

9.3.9 Diffraction

Finally, if $\lambda_s \neq \lambda_t$, there will be some decorrelation because of diffraction. The phase variance due to diffraction is related to the intensity scintillation variance $\sigma^2_{\ln I}$ by

$$\sigma^2_{\phi,r} = G(\lambda_t/\lambda_s)\,\sigma^2_{\ln I}(\lambda_t) \quad , \tag{9.18}$$

with a function G(r), which can be approximated by

$$G(r) \simeq \left(r^{1/2}\,(r-1)\,/2\right)^{4/3} \tag{9.19}$$

for $1 \leq r \lesssim 1.5$ (Colavita, 1992). Observed values for $\sigma^2_{\ln I}$ on Mt. Wilson range from 0.005 to 0.05. The larger of these values gives $\sigma^2_{\phi,r} = 0.0073$, or $\eta = 0.99$ for $\lambda_t = 700\,\mathrm{nm}$, $\lambda_s = 500\,\mathrm{nm}$. Since all stars are affected equally, the calibration procedure takes into account the small coherence loss due to diffraction.

References

M.M. Colavita, *Atmospheric Limitations of a Two-Color Astrometric Interferometer*, Ph.D. thesis, Massachusetts Institute of Technology, Cambridge, MA, USA (1985).

M.M. Colavita, "Phase-referencing for stellar interferometry," in *High-Resolution Imaging by Interferometry II*, J.M. Beckers and F. Merkle, eds. ESO Conference and Workshop Proceedings, **39**, 845–851 (Garching, Germany: European Southern Observatory, 1992).

M.M. Colavita, A.F. Boden, S.L. Crawford, A.B. Meinel, M. Shao, P.N. Swanson, G.T. van Belle, G. Vasisht, J.M. Walker, J.K. Wallace, and P.L. Wizinowich, "The Keck Interferometer," in *Astronomical Interferometry*, R.D. Reasenberg, ed., Proc. SPIE **3350**, 776–784 (1998).

M.M. Colavita, J.K. Wallace, B.E. Hines, Y. Gursel, F. Malbet, D.L. Palmer, X.P. Pan, M. Shao, J.W. Yu, A.F. Boden, P.J. Dumont, J. Gubler, C.D. Koresko, S.R. Kulkarni, B.F. Lane, D.W. Mobley, and G.T. van Belle, "The Palomar Testbed Interferometer," Astrophys. J. **510**, 505–521 (1999).

R.E. Hufnagel, "Variations of atmospheric turbulence," in Digest of Technical Papers Presented at the Topical Meeting on *Optical Propagation through Turbulence*, Wa1–1 – Wa1–4 (Washington, DC: Optical Society of America, 1974).

D. Mozurkewich and J.T. Armstrong, "Array layout and beam combination considerations necessary for imaging with a long baseline optical interferometer," in *High-Resolution Imaging by Interferometry II*, J.M. Beckers and F. Merkle, eds. ESO Conference and Workshop Proceedings, **39**, 801–804 (Garching, Germany: European Southern Observatory, 1992).

D. Mozurkewich, K.J. Johnston, R.S. Simon, P.F. Bowers, R. Gaume, D.J. Hutter, M.M. Colavita, M. Shao, and X.P. Pan, "Angular diameter measurements of stars," Astron. J. **101**, 2207–2219 (1991).

A. Quirrenbach, "Astrometry with the VLT interferometer," in *From Extrasolar Planets to Cosmology: The VLT Opening Symposium*, J. Bergeron and A. Renzini, eds., in press (Berlin, Germany: Springer-Verlag, 2000).

A. Quirrenbach, V. Coudé du Foresto, G. Daigne, K.-H. Hofmann, R. Hofmann, M. Lattanzi, R. Osterbart, R. le Poole, D. Queloz, and F. Vakili, "PRIMA — study for a dual-beam instrument for the VLT Interferometer," in *Astronomical Interferometry*, R.D. Reasenberg, ed., Proc. SPIE **3350**, 807–817 (1998).

A. Quirrenbach, D. Mozurkewich, D.F. Buscher, C.A. Hummel, and J.T. Armstrong, "Phase-referenced visibility averaging in optical long-baseline interferometry," Astron. Astrophys. **286**, 1019–1027 (1994).

A. Quirrenbach, D. Mozurkewich, D.F. Buscher, C.A. Hummel, and J.T. Armstrong, "Angular diameter and limb darkening of Arcturus," Astron. Astrophys. **312**, 160–166 (1996).

M. Shao and M.M. Colavita, "Long-baseline optical and infrared stellar interferometry," Ann. Rev. Astron. Astrophys. **30**, 457–498 (1992).

M. Shao, M.M. Colavita, B.E. Hines, D.H. Staelin, D.J. Hutter, K.J. Johnston, D. Mozurkewich, R.S. Simon, J.L. Hershey, J.A. Hughes, and G.H. Kaplan, "The Mark III stellar interferometer," Astron. Astrophys. **193**, 357–371 (1988).